Received: 00 Month 0000 | Revised: 00 Month 0000 | Accepted: 00 Month 0000

DOI: xxx/xxxx

RESEARCH ARTICLE

MR KLEAN: a Generalized Acquisition-agnostic LLR k-Space Denoising Method for High-dimensional Imaging

Ludwig Sichen Zhao[1,2] | Manuel Taso[3] | Jay A. Gottfried[2,4] | John A. Detre[2,3] | M. Dylan Tisdall[3]

[1]Department of Bioengineering, University of Pennsylvania, Philadelphia, Pennsylvania, USA
[2]Department of Neurology, University of Pennsylvania, Philadelphia, Pennsylvania, USA
[3]Department of Radiology, University of Pennsylvania, Philadelphia, Pennsylvania, USA
[4]Department of Psychology, University of Pennsylvania, Philadelphia, Pennsylvania, USA

Correspondence
M. Dylan Tisdall. Email: mtisdall@pennmedicine.upenn.edu

Funding Information
This work was supported by the National Institutes of Health; awards R01EB031080, R01AG080734 and R01DC018075.

Abstract

Purpose: High-dimensional and dynamic MRI are often limited by thermal noise, particularly in accelerated acquisitions. Although image-domain low-rank denoising methods (e.g., MP-PCA and NORDIC) are effective, reliance on a stationary noise distribution limits applicability to non-Cartesian sampling and advanced reconstruction methods. This work introduces MR KLEAN, a k-space low-rank denoising framework agnostic to acquisition trajectory and reconstruction strategy.

Theory and Methods: MR KLEAN exploits locally low-rank structure in multichannel, high-dimensional k-space. Data are prewhitened using a noise-only calibration scan to enforce independent and identically distributed, zero-mean, unit-variance noise. Casorati matrices are generated through local k-space patches and denoised via singular-value thresholding, with thresholds from Monte-Carlo simulations under known noise statistics. MR KLEAN was evaluated in (1) a phantom study using Cartesian 3D FLASH, (2) an ASL study with spiral readout and compressed sensing reconstruction to assess generalizability and preservation of temporal information via resting-state connectivity analysis, and (3) an accelerated cardiac cine study to assess performance under rapid temporal dynamics.

Results: MR KLEAN increased SNR and CNR in phantom study. In vivo ASL showed reduced noise for perfusion images, improved relative SNR, and substantially enhanced resting-state network detectability and functional connectivity sensitivity. In cardiac imaging, MR KLEAN reduced noise and improved delineation of fine anatomical features while preserving temporal fidelity across cardiac phases.

Conclusion: MR KLEAN provides robust, acquisition- and reconstruction-agnostic k-space denoising, improving image quality and allowing flexible spatial-temporal trade-offs. Results further support that high-dimensional k-space data retain intrinsic low-rank structure analogous to image space despite temporal signal variations.

KEYWORDS:
Denoising, Principal Component Analysis, Thermal Noise

WORD COUNT: 3768

1 | INTRODUCTION

Magnetic Resonance Imaging is a versatile modality for investigating human anatomy and physiology. However, because MRI relies on relatively weak radiofrequency signals, the resulting measurements inherently suffer from low SNR. This problem is exacerbated in high-dimensional or time-resolved (dynamic) imaging, where

maintaining adequate SNR requires trading spatial resolution, temporal resolution, or additional encoding dimensions against SNR or overall acquisition time.

For example, diffusion MRI (dMRI) and BOLD fMRI acquired with EPI are widely used to map brain structural and functional connectivity, respectively. Despite their different contrasts, these rapid imaging modalities both share a fundamental limitation of SNR[1,2,3,4]. Arterial spin labeling (ASL), which directly quantifies cerebral perfusion and serves as an alternative biomarker of brain function to BOLD fMRI, is similarly constrained by its inherent low SNR, even with repeated measurements[5,6,7,8,9]. This limitation is not confined to neuroimaging; other dynamic MRI applications throughout the body can suffer also exhibit low-SNR characteristics due to demands of high temporal resolution, motion robustness, and specific contrast mechanisms[10,11,12,13].

A common strategy to mitigate low SNR is to suppress thermal noise through denoising. Many denoising approaches exploit redundancy in local spatiotemporal image patches, often assuming that repeated measurements form low-rank matrices from which thermal noise can be removed via singular value thresholding[14,15]. Among these, Marchenko–Pastur Principal Component Analysis (MP-PCA) is one of the most widely used methods due to its simplicity and effectiveness[16,17]. MP-PCA integrates local low-rank modeling with random matrix theory to automatically estimate noise variance and determine empirical denoising thresholds. However, it assumes that noise is (1) independent and identically distributed (i.i.d.) and (2) zero-mean. These conditions are often violated in magnitude MR images, particularly when using phased-array coils or parallel imaging reconstruction.

Recently, the Noise Reduction with Distribution Corrected (NORDIC) PCA method has gained considerable attention for effectively removing the thermal noise[3,18]. NORDIC prewhitens the data using a g-factor map and calibrates the PCA threshold using noise-only scans, allowing more accurate noise modeling and delivering substantial improvements in high-resolution BOLD fMRI and dMRI. However, its reliance on g-factor estimation presents challenges for non-linear and iterative reconstruction techniques such as compressed sensing or deep learning. Several variants have been proposed that perform denoising prior to reconstruction, but these remain focused on Cartesian imaging, operate exclusively in image space, and do not fully address the aforementioned limitations[19,20].

In contrast, performing denoising directly in k-space offers greater flexibility and generalizability. Unlike image space, where noise typically becomes spatially varying and correlated after reconstruction, noise in k-space is inherently i.i.d. and zero-mean for single-channel acquisitions. For multichannel data, prewhitening with a noise-only calibration scan ensures i.i.d., zero-mean, unit-variance noise in each channel. These statistical properties allow k-space denoising methods to be applied consistently across a wide range of acquisition trajectories and reconstruction strategies without requiring sequence-specific adaptations such as g-factor maps.

In this work, we propose Magnetic Resonance K-space Local low-rank Estimation for Attenuating Noise (MR KLEAN), a generalized local low-rank (LLR) denoising framework that operates directly in complex-valued k-space prior to any image reconstruction, and is agnostic to both acquisition trajectories and reconstruction methods. Previous studies have demonstrated that local neighborhoods in k-space, for both single- and multichannel acquisitions, exhibit low-rank structure when represented in a block Hankel matrix form[14,21,22,23]. Building upon these findings, we investigate the existence of low-rank representations within local k-space Casorati matrices, analogous to those observed in natural images in the spatial domain. MR KLEAN leverages these properties to preserve low-rank signal components while removing noise levels with known variance and mean.

We evaluated MR KLEAN across different anatomies and k-space trajectories, where existing methods face limitations. MR KLEAN proved to be a robust and generalizable denoising technique for multichannel and high-dimensional MRI. Moreover, the results provide empirical evidence supporting the presence of low-rank structure in k-space. By leveraging this property, MR KLEAN improves SNR without sacrificing spatial or temporal resolution, making it a broadly applicable and effective denoising solution for high-dimensional, low-SNR MRI that is agnostic to both acquisition and reconstruction methods.

2 | THEORY

2.1 | Local Low-rank (LLR) Denoising

For high-dimensional MRI data – such as multiecho acquisitions indexed by TE, dMRI indexed by q-space sampling, or fMRI indexed by time – we denote the image series as $\boldsymbol{m}(\mathbf{r}, \tau)$. Here, $\mathbf{r}$ represents the spatial location in 3D, and $\tau \in \{1, \ldots, N\}$ indexes the images within the set. In the case of multiecho acquisitions, N corresponds to the number of echo times; for dMRI, it refers to the number of q-space samples acquired under varying diffusion weightings; and for fMRI, it represents the

number of time points or volumes collected across the scan duration.

For the LLR denoising method, a patch of size $p_1 \times p_2 \times p_3$ is selected, and the data within each patch are vectorized to form $\mathbf{y}_\tau$. These vectors are then assembled into a Casorati matrix $\mathbf{Y} = [\mathbf{y}_1, \cdots, \mathbf{y}_\tau, \cdots, \mathbf{y}_N] \in \mathbb{C}^{M \times N}$ where $M = p_1 p_2 p_3$ denotes the number of voxels in each patch[24].

The denoising problem is then formulated as:

$$\mathbf{Y} = \mathbf{X} + \epsilon \tag{1}$$

where ϵ represents additive Gaussian noise and $\mathbf{X}$ denotes the underlying noise-free Casorati matrix.

The LLR model assumes that, for a given spatial patch across all N images, $\mathbf{X}$ has a low-rank representation.

Let the singular value decomposition of $\mathbf{Y}$ be:

$$\mathbf{Y} = \mathbf{U} \cdot \mathbf{S} \cdot \mathbf{V}^H \tag{2}$$

where $\mathbf{S}$ is a diagonal matrix containing the ordered singular values λ_i, and $\mathbf{U}$ and $\mathbf{V}$ are unitary matrices comprising the left and right singular vectors, respectively.

To perform LLR denoising and estimate the noise-free matrix $\mathbf{X}$, a threshold λ_{thr} is applied to the singular values. All singular values $\lambda_i < \lambda_{\text{thr}}$ are set to zero, while the remaining values are retained (hard thresholding). Alternatively, soft thresholding may also be applied.

The thresholded diagonal matrix $\widetilde{\mathbf{S}}$ is then used to reconstruct the denoised matrix:

$$\widetilde{\mathbf{Y}} = \mathbf{U} \cdot \widetilde{\mathbf{S}} \cdot \mathbf{V}^H. \tag{3}$$

The final denoised image set is obtained by assembling the denoised patches back to their original spatial locations.

2.2 | Proposed Denoising Method

In a single channel of k-space data, the noise in the k-space data is inherently i.i.d., and zero-mean, thus satisfying the assumptions of random matrix theory. When using phased-array coils, although the noise in the k-space is generally correlated across channels, the noise can be decorrelated through prewhitening and therefore meet i.i.d. and zero-mean conditions. Based on these principles, we propose a generalized denoising method directly in k-space. Let the acquired complex k-space data from channel $j \in \{1, \cdots, C\}$ be denoted by $\boldsymbol{k}_j(\mathbf{r}, \tau)$. $\mathbf{r}$ is the location in 3D k-space, τ indexes the volumes as defined in Section 2.1 and C is the number of channels.

An overview of the proposed MR KLEAN processing pipeline is shown in Figure 1; the individual steps are described in the following subsections.

2.2.1 | Prewhitening

To estimate the noise covariance, a noise scan $\mathbf{Z} \in \mathbb{C}^{M_Z \times C}$ is acquired, where M_Z is the number of noise samples collected from an individual channel. The prewhitened noise data $\mathbf{Z}_w = \mathbf{ZW}$ shall satisfy the following condition:

$$\text{Cov}(\mathbf{Z}_w) = \frac{1}{C-1} {\mathbf{Z}_w}^H \mathbf{Z}_w \tag{4}$$

$$= \frac{1}{C-1} \mathbf{W}^H \mathbf{Z}^H \mathbf{ZW} = \mathbf{I} \tag{5}$$

Therefore, $\mathbf{W}$ can be computed through

$$\mathbf{W} = \frac{1}{\sqrt{C-1}} \mathbf{V}_Z \mathbf{D}^{-\frac{1}{2}} \tag{6}$$

where $\mathbf{Z}^H \mathbf{Z} = \mathbf{V}_Z \mathbf{D} {\mathbf{V}_Z}^H$. $\mathbf{D}$ is the diagonal matrix of eigenvalues of $\mathbf{Z}^H \mathbf{Z}$ and $\mathbf{V}_Z$ is the unitary matrix whose columns are the associated eigenvectors.

The prewhitened k-space image data can therefore be computed and denoted as $\boldsymbol{k}'_j(\mathbf{r}, \tau)$, where the noise is i.i.d., zero-mean, and unit-variance.

2.2.2 | LLR Denoising

Similar to the process described in Section 2.1, within each channel j, for each patch l with a size of $p_1 \times p_2 \times p_3$, at volume τ, data are vectorized into $\mathbf{y}_{\tau,j,l}$. These vectors are then concatenated to generate a Casorati matrix $\mathbf{Y}_l \in \mathbb{C}^{M \times N}$, as follows:

$$\mathbf{Y}_l = \begin{bmatrix} \mathbf{y}_{1,1,l} & \cdots & \mathbf{y}_{\tau,1,l} & \cdots & \mathbf{y}_{N,1,l} \\ \vdots & \ddots & & & \vdots \\ \mathbf{y}_{1,j,l} & & \mathbf{y}_{\tau,j,l} & & \mathbf{y}_{N,j,l} \\ \vdots & & & \ddots & \vdots \\ \mathbf{y}_{1,C,l} & \cdots & \mathbf{y}_{\tau,C,l} & \cdots & \mathbf{y}_{N,C,l} \end{bmatrix} \tag{7}$$

where $M = p_1 p_2 p_3 \cdot C$. As previously mentioned, C denotes the number of acquisition channels and N denotes the number of images within the set.

We first perform singular value decomposition on $\mathbf{Y}_l$:

$$\mathbf{Y}_l = \mathbf{Y}_l \cdot \mathbf{S}_l \cdot {\mathbf{V}_l}^H \tag{8}$$

To denoise the data, we select a threshold λ_l^{thr} and apply hard thresholding to each $\mathbf{S}_l$ to generate $\widetilde{\mathbf{S}}_l$. Therefore, the post-preprocessed denoised Casorati matrix can be obtained through

$$\widetilde{\mathbf{Y}}_l = \mathbf{U}_l \cdot \widetilde{\mathbf{S}}_l \cdot {\mathbf{V}_l}^H \tag{9}$$

To compute the denoised k-space data, we reassemble all patches into their original matrix form, apply the inverse prewhitening transform $\mathbf{W}^{-1}$, and denote the resulting data as $\widetilde{\mathbf{Y}}$.

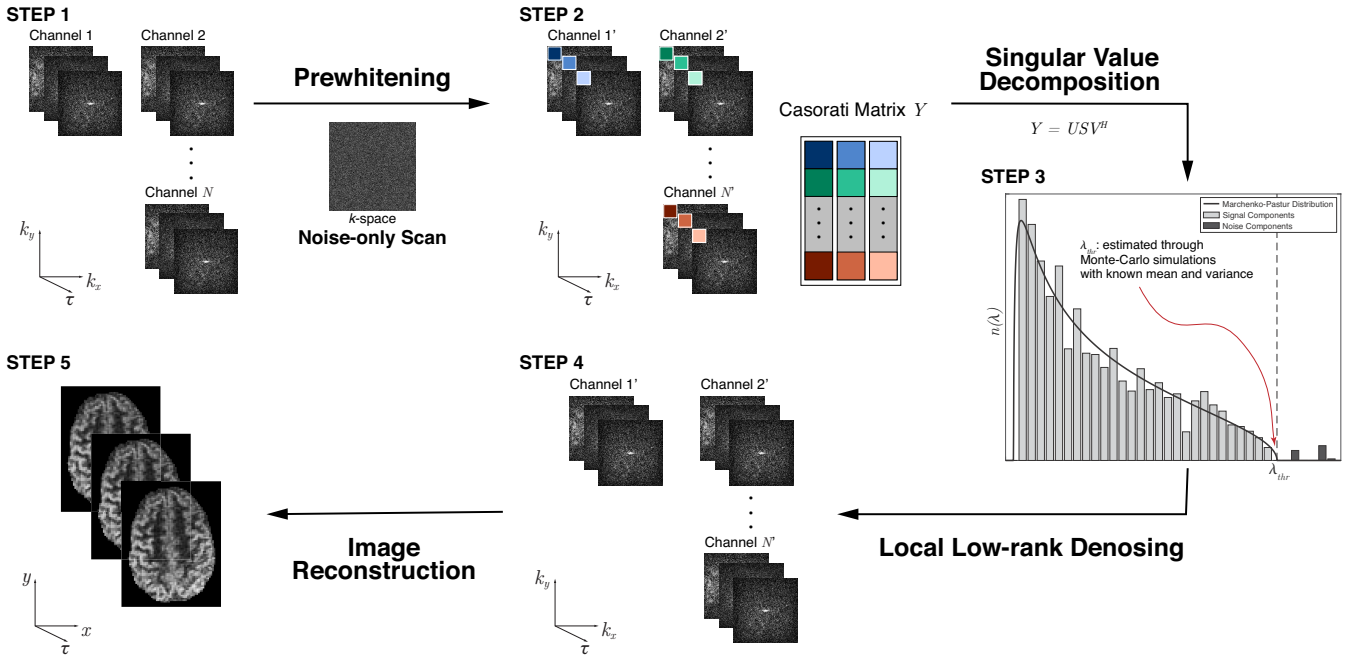

FIGURE 1 Flowchart of the proposed MR KLEAN k-space denoising pipeline. Multichannel k-space data is prewhitened using a noise-only scan (Section 2.2.1), concatenated into Casorati matrices, and denoised via LLR (Section 2.2.2) with a known threshold (Section 2.2.3) to separate signal and noise components prior to image reconstruction.

2.2.3 | Threshold Estimation

For each patch l, the threshold λ_l^{thr} is estimated through Monte-Carlo simulations. We generate a set of random matrices – each having the same dimensions as $\mathbf{Y}_l$ – with entries drawn i.i.d. from a zero mean and unit variance Gaussian distribution. The threshold λ_l^{thr} is then estimated as the sample mean of the largest singular values of these matrices.

3 | METHODS

3.1 | Participants

Two healthy participants provided informed consent under a protocol approved by the University of Pennsylvania Institutional Review Board (IRB #817383): one female (32 years old) for the ASL study and one male (45 years old) for the cardiac study.

3.2 | Phantom Study

We first conducted a phantom study to evaluate the denoising performance of MR KLEAN under stationary conditions using a standard Cartesian readout, isolating the effects of thermal noise without contributions from physiological or motion-related noise sources.

An ACR MRI phantom (JM Specialty Parts, San Diego, CA, USA) was scanned to evaluate MR KLEAN performance under controlled conditions. A 3D FLASH sequence (TR/TE = 6.6/3.3 ms, flip angle = 15 deg, field of view [FOV] = 200 x 200 mm^2, 1.04 mm isotropic resolution, 35 volumes) was acquired on a 3 T MRI scanner (MAGNETOM Prisma, Siemens Healthineers, Erlangen, Germany) using the vendor-provided 20-channel head and neck coil[25]. To simulate varying noise levels, the scan was acquired twice, once with a bandwidth of 360 Hz/pixel and a second time at 1630 Hz/pixel. Three volumes of a noise-only scan were acquired with identical parameters but with the RF pulses disabled.

To quantify denoising performance, we measured SNR and contrast-to-noise ratio (CNR) as a function of the number of averaged volumes for both low and high readout bandwidths, as defined in Section 3.7.1.

We also examined the effect of the number of coil channels on denoising performance: from the same dataset, images were first reconstructed with only a subset of coil channels most relevant to the region of interests (ROIs), after which additional channels were gradually incorporated. Denoising performance was evaluated using relative SNR and relative CNR, defined as the ratio of the metric after to before denoising, computed across all volumes (Section 3.7.1).

3.3 | ASL Study

To demonstrate the generalizability of MR KLEAN, we applied it to ASL data acquired and reconstructed using a non-Cartesian spiral trajectory and compressed-sensing reconstruction. This dataset reflects dynamic brain imaging with slow temporal variations (in this case, cerebral perfusion changes due to resting-state brain activity). We evaluated denoising performance and whether temporal information was preserved by examining both averaged perfusion images and temporal signal characteristics.

ASL data were acquired on a 3 T scanner (MAGNETOM Prisma, Siemens Healthineers, Erlangen, Germany) using the vendor-provided 64-channel head and neck coil with an unbalanced pseudocontinuous ASL (pCASL)[26,27] combined with background-suppressed, 3D accelerated Stack-of-Spirals (SoS) turbo spin echo (TSE) readout[28] (TR/TE = 5000/9.4 ms, labeling duration = 3 s, post-labeling delay = 1.2 s, flip angle = 22.5 deg, G_{max}/G_{avg} = 3.5/0.5 mT/m, 97.5% background suppression, FOV = 220 × 220 mm^2, 2 mm isotropic resolution, 2 shots, 15 label–control pairs). Two volumes of a noise-only scan were also acquired with identical parameters but with the RF pulse disabled.

Fast 3D FLASH scans with matching FOV and resolution (TR/TE = 5/2 ms, bandwidth = 1180 Hz/pixel) were acquired for coil sensitivity estimation[25].

3.4 | Cardiac Study

We applied MR KLEAN to an accelerated cine cardiac acquisition to evaluate its denoising performance under conditions of rapid temporal variation.

Cine cardiac MRI was performed on a 1.5 T scanner (MAGNETOM Avanto^{fit}, Siemens Healthineers, Erlangen, Germany) using the vendor-provided 18-channel body coil in combination with a 32-channel spine coil[29]. Retrospectively ECG-gated, breath-held acquisitions were obtained in the short-axis orientation using a 2D segmented balanced steady-state free precession (bSSFP) sequence (TR/TE = 34.65/1.26 ms, flip angle = 65 deg, FOV = 360 × 270 mm^2, matrix = 240 × 204, slice thickness = 7 mm, 12 slices, bandwidth = 947 Hz/pixel, in-plane GRAPPA acceleration factor = 4 with 44 reference lines). A noise-only scan was acquired using identical parameters, except that only six slices were collected and the RF pulses were disabled.

3.5 | Denoising

MR KLEAN was applied prior to any image reconstruction, following the algorithm described in Section 2.2.

For the 3D FLASH phantom study, the patch size was set to 6 voxels (k_x) × 6 voxels (k_y) × 6 voxels (k_z). For the cardiac study, a patch size of 4 voxels (k_x) × 4 voxels (k_y) × 1 voxel (k_z) was used.

For the ASL study, which used a spiral acquisition, the construction of $\mathbf{y}_\tau$ was modified to account for the acquisition structure. A patch was defined on each spiral arm, consisting of up to 40 consecutive acquired readout points (or fewer if fewer than 40 points remained on the given spiral) across up to 10 consecutive k_z partitions (or fewer if fewer than 10 slices were available). For each coil, $\mathbf{y}_\tau$ was vectorized first along the spiral readout and then along k_z. MR KLEAN was then applied patch by patch on each individual spiral. All label and control images were denoised within the same time series.

3.6 | Image Reconstruction

All images were reconstructed offline from raw k-space data using MATLAB (R2020b, The MathWorks Inc., Natick, MA, USA). For both the 3D FLASH phantom study and the cine cardiac study, coil channels were sum-of-squares combined. For ASL data, coil sensitivities were first estimated from the 3D FLASH data using ESPIRiT (σ = 0.9, c = 0.01)[30]. The images were then reconstructed using a locally low-rank regularized compressed sensing (CS) approach[31] (λ = 0.001, 100 iterations) implemented in the BART toolbox (0.9.00)[32,33]. The reconstructed ASL volumes were subsequently motion-corrected using FSL (6.0.6.2, FMRIB Software Library, University of Oxford, Oxford, UK)[34]. Perfusion-weighted images were then generated by subtracting the label volume from the corresponding control volume.

3.7 | Data Analysis

3.7.1 | SNR, Relative SNR, CNR and Relative CNR

For each acquired 4D image series $\boldsymbol{m}(\mathbf{r}, \tau)$, as defined in Section 2.1, we first averaged across the volumes (indexed by τ) to obtain a single mean 3D image for subsequent analysis.

SNR was computed within an ROI as the ratio of the mean signal intensity to the standard deviation of the

signal across voxels in the ROI:

$$\mathrm{SNR} = \frac{\overline{x}_{\mathrm{ROI}}}{\sigma_{\mathrm{ROI}}}. \tag{10}$$

Relative SNR was defined as the ratio of SNR values between two image series computed within the same ROI.

CNR was computed as

$$\mathrm{CNR} = \frac{\overline{x}_{\mathrm{signal}} - \overline{x}_{\mathrm{background}}}{\sqrt{\frac{\sigma^2_{\mathrm{signal}} + \sigma^2_{\mathrm{background}}}{2}}}, \tag{11}$$

where $\overline{x}_{\mathrm{signal}}$ and $\overline{x}_{\mathrm{background}}$ denote the mean intensities within the predefined signal and background regions, respectively, and $\sigma^2_{\mathrm{signal}}$ and $\sigma^2_{\mathrm{background}}$ are the corresponding variances across voxels within those regions.

Relative CNR was defined as the ratio of CNR values between two image series computed using the same signal and noise regions.

3.7.2 | Seed-Based Connectivity (SBC) Maps

For the ASL study, SBC maps were computed by first extracting the mean time series from the perfusion images within the ROI. The voxel-wise Pearson correlation coefficient (r) between the ROI time series and the time series of each voxel was then calculated across all volumes to generate the connectivity map.

The seed region was the right posterior cingulate cortex (PCC). Accordingly, the ROI was defined as a 6-mm-radius sphere centered at (0, -53, 26) in Montreal Neurological Institute (MNI) space, consistent with prior work[35,36]. The MNI template (ICBM 152 Nonlinear Asymmetrical, version 2009c; MNI-ICBM2009c)[37,38] was registered to the subject's ASL proton density (M0) image[39] using Advanced Normalization Tools (ANTs, 2.3.5)[40,41] to estimate the spatial transformation, which was then applied to warp the ROI from MNI space into subject space.

4 | RESULTS

4.1 | Phantom Study

Figure 2A demonstrates a representative volume before and after denoising. Visually, MR KLEAN reduces background grain and more clearly delineates fine structural features. Quantitative results are shown in Figures 2B and 2C: as expected, increasing the readout bandwidth led to noisier images, whereas SNR and CNR increased with the number of volumes averaged and eventually approached a plateau.

For single-volume acquisitions, MR KLEAN provided minimal improvement in SNR at either bandwidth. In contrast, with two or more volumes, MR KLEAN produced substantial SNR gains, particularly at the higher readout bandwidth. With additional volumes being averaged, the SNR improvement increased further, plateauing at approximately 18 volumes for the low-bandwidth condition, while continuing to increase for the high-bandwidth condition.

CNR followed a similar trend. Overall, the low-bandwidth acquisition yielded higher CNR, and MR KLEAN further increased CNR as the number of averaged volumes increased. Although improvements were minimal for single-volume data, substantial gains were observed for multivolume acquisitions, demonstrating effective suppression of thermal noise. Notably, for the low bandwidth condition, the CNR measured after denoising with 8 volumes was approximately comparable to that obtained with 20 volumes before denoising, suggesting that MR KLEAN could effectively reduce the required acquisition time by more than half.

Finally, Figure 2D shows that both relative SNR and relative CNR increased consistently with the number of coil channels. Even when restricted to the single channel most relevant to the ROIs, MR KLEAN remained effective, yielding a relative CNR of 1.64 and a relative SNR of 1.45.

4.2 | ASL Study

Figure 3A shows representative perfusion images before and after denoising across varying numbers of averaged label–control pairs, while Figure 3B presents the corresponding quantitative analysis using relative SNR for both cortical and white matter regions. Similar to the phantom study, a single-volume perfusion image provided a limited opportunity for denoising. However, with two or more volumes, MR KLEAN achieved noticeable noise suppression, resulting in an improved perfusion image and SNR.

To evaluate the impact of MR KLEAN on temporal dynamics, we next examined functional connectivity of the resting-state by seeding the right PCC and computing voxel-wise correlation maps before and after denoising (Figure 4). Without denoising, connectivity was weak and spatially confined. In contrast, after applying MR KLEAN, clear network patterns emerged that closely resembled the default mode network (DMN), indicating that MR KLEAN not only preserved temporal information but also improved sensitivity to physiologically significant fluctuations in brain activity.

These results show that MR KLEAN effectively improves both the spatial quality and the sensitivity of the temporal dynamics of ASL data acquired

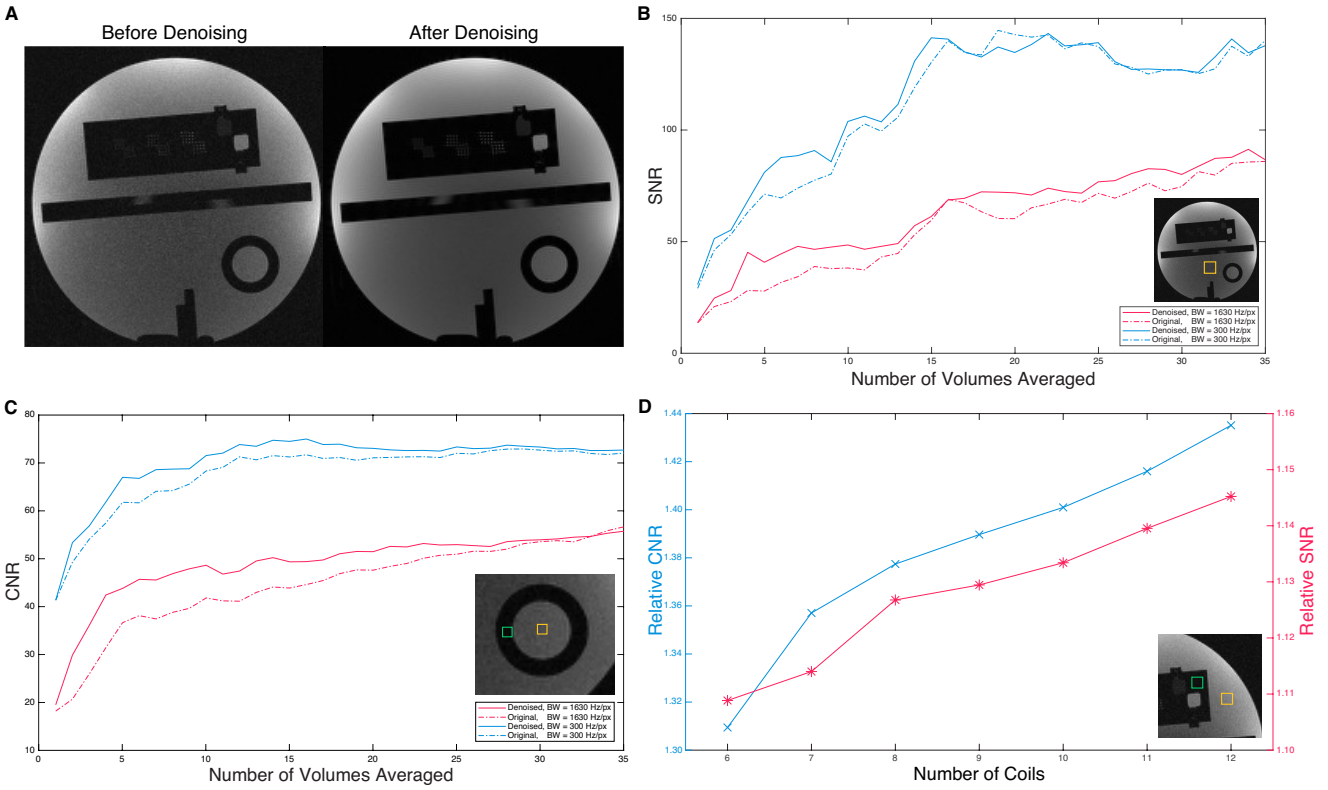

FIGURE 2 Comparison of images before and after denoising in the phantom study. A) A representative slice from a single volume of the ACR phantom before and after applying MR KLEAN across all 35 volumes. B) SNR before (dashed lines) and after (solid lines) applying MR KLEAN for different numbers of averaged volumes at low readout bandwidth (300 Hz/pixel, blue) and high readout bandwidth (1630 Hz/pixel, red). The ROI used for SNR measurement is indicated by the yellow square in the inset. C) CNR before (dashed lines) and after (solid lines) applying MR KLEAN for different numbers of averaged volumes at low readout bandwidth (300 Hz/pixel, blue) and high readout bandwidth (1630 Hz/pixel, red). The signal and background ROIs used for CNR estimation are shown as yellow and green squares, respectively, in the inset. D) Relative SNR (ratio of SNR after to before applying MR KLEAN to all volumes, red) and relative CNR (ratio of CNR after to before applying MR KLEAN to all volumes, blue) for the high readout bandwidth (1630 Hz/pixel) across different numbers of coil channels. The inset shows the ROIs used for measurements: the yellow square denotes the ROI for SNR measurement and the signal region for CNR estimation, while the green square indicates the background region used for CNR estimation.

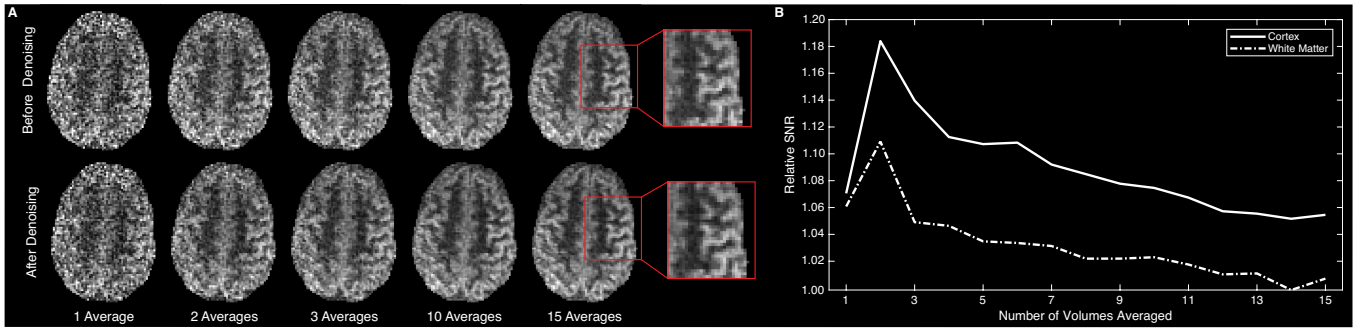

FIGURE 3 Comparison of Images before and after denoising in the ASL study. A) A representative slice of perfusion-weighted images averaged over different numbers of label–control pairs, shown before (top row) and after (bottom row) MR KLEAN denoising. B) Relative SNR (ratio of SNR after to before applying MR KLEAN) across different numbers of averaged label–control pairs for cortex and white matter regions in the representative slice.

with spiral readouts, demonstrating a generalizability to non-Cartesian, dynamic imaging applications.

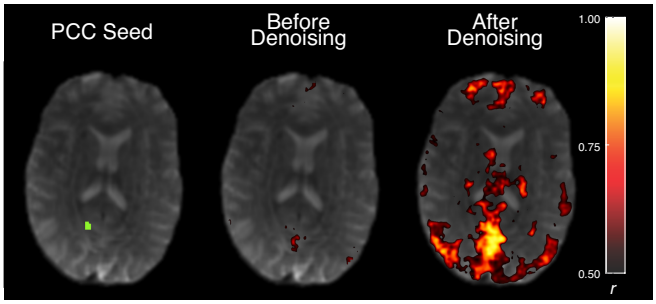

FIGURE 4 Seed-based connectivity before and after denoising. The seed region is shown in green in the right posterior cingulate cortex.

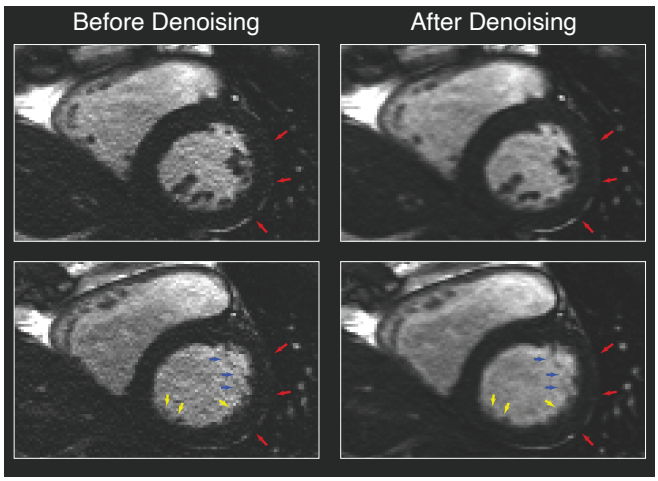

FIGURE 5 Comparison of images before and after denoising in the cardiac study. Three consecutive short-axis slices from a single cine volume are shown before and after applying MR KLEAN. Pre-scan normalization was applied for visualization purposes. Red arrows: epicardium. Blue arrows: papillary muscle. Yellow arrows: ventricular trabeculae.

4.3 | Cardiac Study

Figure 5 shows three consecutive short-axis slices from a cine cardiac scan before and after denoising, demonstrating that MR KLEAN improves image quality under rapid temporal variation. Visually, MR KLEAN substantially reduced noise, particularly in the myocardium, while preserving anatomical detail and enhancing the definition of epicardium (red arrows), papillary muscles (blue arrows) and ventricular trabeculae (yellow arrows). A motion clip demonstrating the same three slices across all 23 cardiac phases is provided in Supporting Information Video S1, showing that MR KLEAN effectively removes noise from individual volumes while preserving the temporal fidelity of cardiac motion.

5 | DISCUSSION

In this work, we generalized the NORDIC framework to k-space while preserving its core principles. Specifically, we hypothesized that multivolume k-space data also exhibited a low-rank structure and that thermal noise can be effectively removed by thresholding singular values according to known noise statistics. Similar to NORDIC, multichannel data were first prewhitened using noise-only calibration scans to satisfy zero-mean, unit-variance, and i.i.d. noise characteristics. The LLR model was then applied to the k-space data, with the threshold determined by Monte-Carlo simulations based on zero-mean, unit-variance Gaussian noise.

We demonstrated the performance of MR KLEAN through three experiments designed to evaluate its effectiveness and robustness under progressively more complex imaging conditions. First, as shown in Figure 2, MR KLEAN effectively removed thermal noise and improved image quality in a controlled phantom study, free from physiological noise or motion effects. Next, an ASL study (Figures 3 and 4) demonstrated two key advantages of MR KLEAN: (1) its generalizability across non-linear and iterative reconstruction methods, and (2) its ability to preserve and improve temporal dynamics in data with stationary spatial structures. Lastly, we extended our evaluation to dynamic imaging scenarios using an accelerated bSSFP cine cardiac scan (Figure 5). Despite rapid temporal changes in cardiac motion, MR KLEAN effectively suppressed noise within each time frame while maintaining temporal fidelity, demonstrating that the method does not introduce blurring across the temporal dimension. Collectively, these results highlight the versatility and robustness of MR KLEAN across acquisition strategies, readout trajectories, and temporal dynamics. Moreover, these findings provide strong evidence supporting our hypothesis that multivolume k-space data, regardless of the temporal changes, exhibit a low-rank structure analogous to that observed in the image space.

When examining the effect of the number of volumes, we observed consistent trends in Figures 2B and 2C. For a single-volume acquisition, the SNR and CNR are identical before and after denoising. However, as more volumes are incorporated, the denoised images rapidly exceed the original SNR and CNR, with the improvement gradually approaching the levels obtained through conventional averaging. A similar trend can be found in Figure 3C, where the relative SNR equals 1 for a single volume, increases sharply with the addition of only a few volumes, and eventually converges to the value achieved through averaging alone.

These results can be explained by considering Eq. 7. When the number of volumes is limited, the Casorati

matrix $\mathbf{Y}_l \in \mathbb{C}^{m\times n}$ becomes tall ($m \gg n$), degrading the separation between signal and noise singular values. In the extreme case where $n = 1$, $\mathbf{Y}_l$ contains only a single singular value, making it impossible for denoising to isolate a noise-only component; consequently, no meaningful denoising can be achieved. As additional volumes are incorporated, the separation between signal and noise improves, more ranks can be retained, and MR KLEAN becomes increasingly effective.

Finally, we examined the effect of the number of coil channels on MR KLEAN's denoising performance (Figure 2D). The results demonstrate that although MR KLEAN can operate effectively on single-channel data, incorporating additional coil channels further improves denoising performance. This suggests that multichannel information increases the intrinsic low-rank structure of the data and thus improves the effectiveness of MR KLEAN. Therefore, these results indicate that MR KLEAN benefits from both multi-coil and high-dimensional data, resulting in robust denoising performance even under conditions of rapid variation across the additional dimensions.

It is worth noting that while MR KLEAN is evaluated using high-dimensional (4D) imaging datasets in this study, its framework is equally applicable to three-dimensional acquisitions if acquired with multiple repetitions. For example, 3D structural or quantitative imaging protocols that rely on averaging – such as repeated short T_1-weighted scans shown by Elliott et al. to improve precision in brain morphometry through repetition averaging – could also benefit from MR KLEAN denoising applied across repeated volumes[42].

In addition, as MR KLEAN operates directly on raw k-space data prior to any image reconstruction, with the acquisition of a brief noise scan, it can be readily integrated into existing online scanner reconstruction pipelines to provide direct improvements in image quality without requiring any changes to downstream workflows or acquisition parameters.

While MR KLEAN has demonstrated remarkable and versatile denoising performance, several questions remain open for future investigation. As with other LLR-based methods, the selection of the optimal patch size remains heuristic and warrants systematic evaluation[43,44,45]. In this study, the Casorati matrix for Cartesian acquisitions was constructed following the conventional approach used in MP-PCA and NORDIC. For non-Cartesian acquisitions, such as the spiral readout in the ASL study, the patch construction was adapted to account for the sampling geometry. Nevertheless, additional optimization and validation of the non-Cartesian patch design are needed, despite the strong empirical performance observed in this work.

6 | CONCLUSIONS

MR KLEAN is a generalized low-rank denoising method that operates directly in k-space, extending the applicability of LLR-based denoising beyond conventional acquisition methods and image-space implementations. Taking advantage of the inherent statistical structure of high-dimensional and multichannel MRI data, MR KLEAN consistently suppresses thermal noise across diverse acquisition schemes while preserving spatial detail and temporal fidelity. In this study, we demonstrated its effectiveness in phantom, ASL, and cardiac imaging, further highlighting its robustness in varying contrast mechanisms, sampling trajectories, reconstruction strategies, and temporal dynamics. Collectively, these results establish MR KLEAN as a robust, acquisition- and reconstruction-agnostic denoising method that is broadly and easily applicable to high-dimensional MRI acquisitions and may help mitigate image-quality degradation in accelerated imaging.

ACKNOWLEDGMENTS

This work was supported by the National Institutes of Health under awards R01EB031080, R01AG080734, and R01DC018075. We thank the Center for Advanced Magnetic Resonance Imaging and Spectroscopy, RRID: SCR_022398, for their assistance with the MRI portion of the research. MT was employed by Siemens Medical Solutions USA during part of this work.

Data Availability Statement

The source code and scripts used in this work are publicly available at https://github.com/luxwig/MR-CLEAN and archived at DOI:10.5281/zenodo.18311381. The software revision used for the results reported in this manuscript is SHA-1: 5f8bc99a9eaf8bf11ebbbe9ff8c368119f0c33a7.

ORCID

Ludwig Sichen Zhao 0000-0001-5469-996X
Manuel Taso 0000-0003-2405-9165
Jay A. Gottfried 0009-0002-0787-8513
John A. Detre 0000-0002-8115-6343
M. Dylan Tisdall 0000-0002-0454-3112

REFERENCES

1. Jones Derek K. Challenges and limitations of quantifying brain connectivity in vivo with diffusion MRI. *Imaging in Medicine.* 2010;2(3):341–355.
2. Manzano Patron Jose Pedro, Moeller Steen, Andersson Jesper L.R., Ugurbil Kamil, Yacoub Essa, Sotiropoulos Stamatios N.. Denoising diffusion MRI: Considerations and implications for analysis. *Imaging Neuroscience.* 2024;2:imag–2–00060.
3. Vizioli Luca, Moeller Steen, Dowdle Logan, et al. Lowering the thermal noise barrier in functional brain mapping with magnetic resonance imaging. *Nature Communications.* 2021;12(1):5181.
4. Triantafyllou Christina, Polimeni Jonathan R., Wald Lawrence L.. Physiological noise and signal-to-noise ratio in fMRI with multi-channel array coils. *NeuroImage.* 2011;55(2):597–606.
5. Hernandez-Garcia Luis, Aramendía-Vidaurreta Verónica, Bolar Divya S., et al. Recent Technical Developments in ASL: A Review of the State of the Art. *Magnetic Resonance in Medicine.* 2022;88(5):2021–2042.
6. Alsop David C., Detre John A., Golay Xavier, et al. Recommended implementation of arterial spin-labeled perfusion MRI for clinical applications: A consensus of the ISMRM perfusion study group and the European consortium for ASL in dementia. *Magnetic Resonance in Medicine.* 2015;73(1):102–116.
7. Garcia Dairon M., Duhamel Guillaume, Alsop David C.. Efficiency of inversion pulses for background suppressed arterial spin labeling. *Magnetic Resonance in Medicine.* 2005;54(2):366–372.
8. Detre John A., Wang Jiongjiong. Technical aspects and utility of fMRI using BOLD and ASL. *Clinical Neurophysiology.* 2002;113(5):621–634.
9. Detre John A., Leigh John S., Williams Donald S., Koretsky Alan P.. Perfusion imaging. *Magnetic Resonance in Medicine.* 1992;23(1):37–45.
10. Raptis Constantine A., Ludwig Daniel R., Hammer Mark M., et al. Building blocks for thoracic MRI: Challenges, sequences, and protocol design. *Journal of Magnetic Resonance Imaging.* 2019;50(3):682–701.
11. Wieben Oliver, Francois Christopher, Reeder Scott B.. Cardiac MRI of ischemic heart disease at 3 T: Potential and challenges. *European Journal of Radiology.* 2008;65(1):15–28.
12. Rajiah Prabhakar Shantha, François Christopher J., Leiner Tim. Cardiac MRI: State of the Art. *Radiology.* 2023;307(3):e223008.
13. Wen H., Denison T. J., Singerman R. W., Balaban R. S.. The Intrinsic Signal-to-Noise Ratio in Human Cardiac Imaging at 1.5, 3, and 4 T. *Journal of Magnetic Resonance.* 1997;125(1):65–71.
14. Haldar Justin P.. Low-Rank Modeling of Local k-Space Neighborhoods (LORAKS) for Constrained MRI. *IEEE Transactions on Medical Imaging.* 2014;33(3):668–681.
15. Xu Lin, Wang Changqing, Chen Wufan, Liu Xiaoyun. Denoising Multi-Channel Images in Parallel MRI by Low Rank Matrix Decomposition. *IEEE Transactions on Applied Superconductivity.* 2014;24(5):1–5.
16. Veraart Jelle, Novikov Dmitry S., Christiaens Daan, Ades-aron Benjamin, Sijbers Jan, Fieremans Els. Denoising of diffusion MRI using random matrix theory. *NeuroImage.* 2016;142:394–406.
17. Veraart Jelle, Novikov Dmitry S., Christiaens Daan, Ades-aron Benjamin, Sijbers Jan, Fieremans Els. Denoising of diffusion MRI using random matrix theory. *NeuroImage.* 2016;142:394–406.
18. Moeller Steen, Pisharady Pramod Kumar, Ramanna Sudhir, et al. NOise reduction with DIstribution Corrected (NORDIC) PCA in dMRI with complex-valued parameter-free locally low-rank processing. *NeuroImage.* 2021;226:117539.
19. Demirel Omer, Moeller Steen, Vizioli Luca, et al. High-Quality 0.5mm Isotropic Functional MRI Using a Synergistic Combination of NORDIC Denoising and Deep Learning Reconstruction. In: *Proceedings of the Joint Annual Meeting ISMRM-ESMRMB & ISMRT Annual Meeting*, International Society for Magnetic Resonance in Medicine; 2022:3950; London, England, UK.
20. Moeller Steen, Olman Cheryl, Vizioli Luca, et al. NORDIC denoising before image reconstruction. In: *Proceedings of the 2021 ISMRM & SMRT Annual Meeting & Exhibition*, International Society for Magnetic Resonance in Medicine; 2021.
21. Haldar Justin P., Zhuo Jingwei. P-LORAKS: Low-rank modeling of local k-space neighborhoods with parallel imaging data. *Magnetic Resonance in Medicine.* 2016;75(4):1499–1514.
22. Shin Peter J., Larson Peder E. Z., Ohliger Michael A., et al. Calibrationless parallel imaging reconstruction based on structured low-rank matrix completion. *Magnetic Resonance in Medicine.* 2014;72(4):959–970.
23. Lee Dongwook, Jin Kyong Hwan, Kim Eung Yeop, Park Sung-Hong, Ye Jong Chul. Acceleration of MR parameter mapping using annihilating filter-based low rank hankel matrix (ALOHA). *Magnetic Resonance in Medicine.* 2016;76(6):1848–1864.
24. Howard James D., Kahnt Thorsten, Gottfried Jay A.. Converging prefrontal pathways support associative and perceptual features of conditioned stimuli. *Nature Communications.* 2016;7(1):11546.
25. Haase A, Frahm J, Matthaei D, Hanicke W, Merboldt K. D. FLASH imaging. Rapid NMR imaging using low flip-angle pulses. *Journal of Magnetic Resonance (1969).* 1986;67(2):258–266.
26. Dai Weiying, Garcia Dairon, Bazelaire Cedric, Alsop David C.. Continuous flow-driven inversion for arterial spin labeling using pulsed radio frequency and gradient fields. *Magnetic Resonance in Medicine.* 2008;60(6):1488–1497.
27. Zhao Moss Y., Mezue Melvin, Segerdahl Andrew R., et al. A systematic study of the sensitivity of partial volume correction methods for the quantification of perfusion from pseudo-continuous arterial spin labeling MRI. *NeuroImage.* 2017;162:384–397.
28. Chang Yulin V., Vidorreta Marta, Wang Ze, Detre John A.. 3D-accelerated, stack-of-spirals acquisitions and reconstruction of arterial spin labeling MRI. *Magnetic Resonance in Medicine.* 2017;78(4):1405–1419.

29. Carr James C., Simonetti Orlando, Bundy Jeff, Li Debiao, Pereles Scott, Finn J. Paul. Cine MR Angiography of the Heart with Segmented True Fast Imaging with Steady-State Precession. *Radiology.* 2001;219(3):828–834.
30. Uecker Martin, Lai Peng, Murphy Mark J., et al. ESPIRiT—an eigenvalue approach to autocalibrating parallel MRI: Where SENSE meets GRAPPA. *Magnetic Resonance in Medicine.* 2014;71(3):990–1001.
31. Lustig Michael, Donoho David, Pauly John M.. Sparse MRI: The application of compressed sensing for rapid MR imaging. *Magnetic Resonance in Medicine.* 2007;58(6):1182–1195.
32. Blumenthal Moritz, Heide Martin, Holme Christian, et al. *mrirecon/bart: version 0.9.00.* 2023.
33. Uecker Martin, Ong Frank, Tamir Jonathan I., et al. Berkeley advanced reconstruction toolbox. In: *Proc. Intl. Soc. Mag. Reson. Med.*, International Society for Magnetic Resonance in Medicine; 2015:9; Toronto, ON, Canada.
34. Jenkinson Mark, Bannister Peter, Brady Michael, Smith Stephen. Improved Optimization for the Robust and Accurate Linear Registration and Motion Correction of Brain Images. *NeuroImage.* 2002;17(2):825–841.
35. Andrews-Hanna Jessica R., Snyder Abraham Z., Vincent Justin L., et al. Disruption of Large-Scale Brain Systems in Advanced Aging. *Neuron.* 2007;56(5):924–935.
36. Van Dijk Koene R. A., Hedden Trey, Venkataraman Archana, Evans Karleyton C., Lazar Sara W., Buckner Randy L.. Intrinsic Functional Connectivity As a Tool For Human Connectomics: Theory, Properties, and Optimization. *Journal of Neurophysiology.* 2010;103(1):297–321.
37. Fonov VS, Evans AC, McKinstry RC, Almli CR, Collins DL. Unbiased nonlinear average age-appropriate brain templates from birth to adulthood. *NeuroImage.* 2009;47:S102.
38. Fonov Vladimir, Evans Alan C., Botteron Kelly, Almli C. Robert, McKinstry Robert C., Collins D. Louis. Unbiased average age-appropriate atlases for pediatric studies. *NeuroImage.* 2011;54(1):313–327.
39. Suzuki Yuriko, Clement Patricia, Dai Weiying, et al. ASL lexicon and reporting recommendations: A consensus report from the ISMRM Open Science Initiative for Perfusion Imaging (OSIPI). *Magnetic Resonance in Medicine.* 2024;91(5):1743–1760.
40. Avants B. B., Epstein C. L., Grossman M., Gee J. C.. Symmetric diffeomorphic image registration with cross-correlation: Evaluating automated labeling of elderly and neurodegenerative brain. *Medical Image Analysis.* 2008;12(1):26–41.
41. Tustison Nicholas J., Cook Philip A., Holbrook Andrew J., et al. The ANTsX ecosystem for quantitative biological and medical imaging. *Scientific Reports.* 2021;11(1):9068.
42. Elliott Maxwell L., Nielsen Jared A., Hanford Lindsay C., et al. Precision brain morphometry using cluster scanning. *Imaging Neuroscience.* 2024;2:imag–2–00175.
43. Pfaffenrot Viktor, Norris David. Validating NORDIC denoising on high-resolution fMRI data at 7 T. In: *Proceedings of 2023 ISMRM & ISMRT Annual Meeting*, International Society for Magnetic Resonance in Medicine; 2023:2719; Toronto, ON, Canada.
44. Olesen Jonas L., Ianus Andrada, Østergaard Leif, Shemesh Noam, Jespersen Sune N.. Tensor denoising of multidimensional MRI data. *Magnetic Resonance in Medicine.* 2023;89(3):1160–1172.
45. Faes Lonike K., Lage-Castellanos Agustin, Valente Giancarlo, et al. Evaluating the effect of denoising submillimeter auditory fMRI data with NORDIC. *Imaging Neuroscience.* 2024;2:imag–2–00270.

SUPPORTING INFORMATION

The following supporting information is available as part of the online article:

Supporting Information Video S1 Video of cine images obtained before and after denoising. Two representative cardiac cine slices are shown before (left) and after (right) denoising.